Article

Toughening mechanisms of the elytra of the diabolical ironclad beetle

https://doi.org/10.1038/s41586-020-2813-8

Received: 6 August 2019

Accepted: 18 August 2020

Published online: 21 October 2020

Check for updates

Jesus Rivera[1], Maryam Sadat Hosseini[2], David Restrepo[2,3], Satoshi Murata[4], Drago Vasile[5], Dilworth Y. Parkinson[6], Harold S. Barnard[6], Atsushi Arakaki[4], Pablo Zavattieri[2] & David Kisailus[1,5,7]✉

Joining dissimilar materials such as plastics and metals in engineered structures remains a challenge[1]. Mechanical fastening, conventional welding and adhesive bonding are examples of techniques currently used for this purpose, but each of these methods presents its own set of problems[2] such as formation of stress concentrators or degradation under environmental exposure, reducing strength and causing premature failure. In the biological tissues of numerous animal and plant species, efficient strategies have evolved to synthesize, construct and integrate composites that have exceptional mechanical properties[3]. One impressive example is found in the exoskeletal forewings (elytra) of the diabolical ironclad beetle, *Phloeodes diabolicus*. Lacking the ability to fly away from predators, this desert insect has extremely impact-resistant and crush-resistant elytra, produced by complex and graded interfaces. Here, using advanced microscopy, spectroscopy and in situ mechanical testing, we identify multiscale architectural designs within the exoskeleton of this beetle, and examine the resulting mechanical response and toughening mechanisms. We highlight a series of interdigitated sutures, the ellipsoidal geometry and laminated microstructure of which provide mechanical interlocking and toughening at critical strains, while avoiding catastrophic failure. These observations could be applied in developing tough, impact- and crush-resistant materials for joining dissimilar materials. We demonstrate this by creating interlocking sutures from biomimetic composites that show a considerable increase in toughness compared with a frequently used engineering joint.

For millions of years, environmental pressures and predator–prey relationships have driven arthropods to develop structures that are both mechanically robust and multifunctional. With over 350,000 species of flying, terrestrial and aquatic variants, beetle cuticles exemplify these traits by providing structural support, water collection and retention, and serve as a defence mechanism against predators[4–8]. In particular, the Zopherinae ('ironclad') family of terrestrial insects are known among entomologists for their compression resistance and for the ability of their hardened forewings or elytra to bend steel mounting pins (Fig. 1b)[9]. Evolved from flying ancestors, these beetles no longer possess the agile means of evasion that result from membranous hindwings[10–12]. Instead, they adapted a robust exoskeleton with elytra (density 0.97 g cm^{-3}, compared with 0.51 g cm^{-3} for the flying beetle *Trypoxylus dichotomus*) that are fused by a robust interface[13]. We describe the multifunctional exoskeleton of the diabolical ironclad beetle (DIB), *Phloeodes diabolicus* (also known as *Nosoderma diabolicum*), an oak-dwelling fungivore primarily residing on the western coast of North America. This beetle can be found under the bark of hardwood and coniferous trees[9], playing dead and superficially resembling a small rock because of the rough texture of its elytra[14]. Beyond feigning death, this beetle has a remarkable ability to withstand crushing and piercing strikes from predators, and even the occasional automobile.

Mechanical and structural characterization

To assess the resistance of *P. diabolicus* to external loads possibly encountered in its natural habitat, we performed compression tests on its entire exoskeleton and compared the maximum compressive strength with that of other beetles native to the southern California region (Fig. 1, Extended Data Figs. 1 and 2). Other terrestrial beetles (*Asbolus verrucosus*, *Eleodes grandicollis* and *Cryptoglossa muricata*) with similar predation (that is, via crushing and pecking), defence by playing dead (thanatosis) and habitat were selected for comparison[15–17]. At the onset of compression, *P. diabolicus* exhibits a change in stiffness from 115 N mm^{-1} to 291 N mm^{-1} at 0.64 mm displacement (Fig. 1c, Extended Data Fig. 1a) and fractures at a maximum force of 149 N with an average load of 133 ± 16 N (~39,000 times its body weight), significantly greater than the force an adult human can generate by pressing the thumb and index finger together (43.0 ± 18.4 N)[18]. By contrast, the other beetles can only withstand an average peak load of less than 68 N and have a lower strength-to-weight ratio (Fig. 1c, inset).

[1]Materials Science and Engineering Program, University of California, Riverside, CA, USA. [2]Lyles School of Civil Engineering, Purdue University, West Lafayette, IN, USA. [3]Department of Mechanical Engineering, The University of Texas at San Antonio, San Antonio, TX, USA. [4]Institute of Global Innovation Research, Tokyo University of Agriculture and Technology, Koganei, Tokyo, Japan. [5]Department of Chemical and Environmental Engineering, University of California, Riverside, CA, USA. [6]Advanced Light Source, Lawrence Berkeley National Laboratory, Berkeley, CA, USA. [7]Department of Materials Science and Engineering, University of California, Irvine, CA, USA. ✉e-mail: david.k@uci.edu

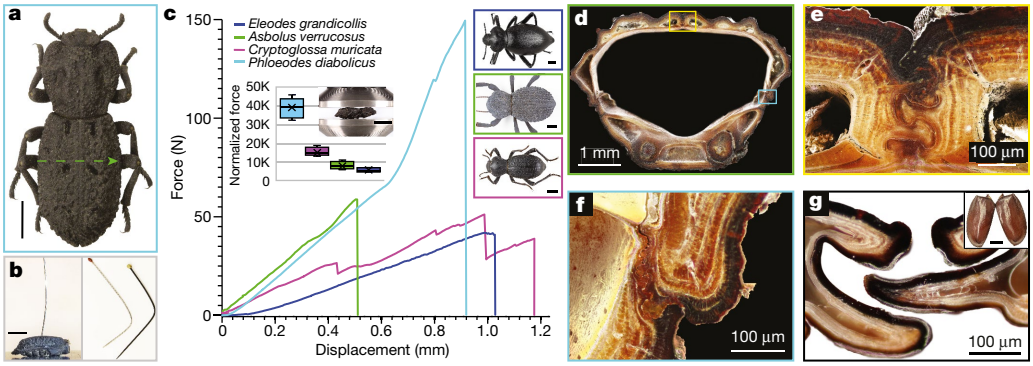

Fig. 1 | Mechanical properties of terrestrial beetles and architectural features of DIB (*P. diabolicus*). **a**, Image of DIB. Scale bar, 5 mm. **b**, Image of steel pin bent by elytra of the DIB. Scale bar, 5 mm. **c**, Representative force versus displacement curves for beetles tested under compression. Inset, box plots showing median and standard deviation of normalized maximum load (force/weight of beetle); number of specimens $N = 5$. Additional beetles tested in compression (top to bottom): *E. grandicollis*, *A. verrucosus* and *C. muricata*. Scale bars, 5 mm. **d**–**f**, Optical micrographs of a transverse cross-section of DIB (**d**), indicating the interfacial architectural regions of interest: medial sutures (**e**) and lateral supports (**f**). **g**, Cross-sectional optical micrograph of suture of a Japanese flying beetle, *Trypoxylus dichotomus*. Inset, elytra of *T. dichotomus*. Scale bar, 10 mm.

Asbolus verrucosus exhibited a similar initial stiffness to *P. diabolicus* but fractured at about 50% of the strain, suggesting a variation in composition or design features within the exoskeleton.

Beyond microstructural, nanomechanical and compositional analysis of the bulk of the elytra (Extended Data Figs. 1b–e, 2, and Methods), two additional and distinct features are observed within its exoskeleton: a medial suture that permanently fuses the two elytra together (Fig. 1e), and lateral interfaces that connect and support the elytra to the ventral cuticle (Fig. 1f). The medial suture consists of interdigitated 'jigsaw' arrangements of protruding segments, called blades, along the length of the abdomen (Supplementary Video 1). Evaluation of the DIB's flying relatives reveals a tongue-and-groove design (Fig. 1g) that enables actuation and flight. Comparative analyses between the sutures and lateral interfaces of multiple terrestrial species show substantial differences in the thickness and degree of interdigitation, with the greatest number of interlocking elements found in *P. diabolicus* (Extended Data Fig. 3). However, there has been relatively little research into variations of these protective interlocking interfaces in beetles[19].

Lateral supports

In terrestrial habitats, these beetles often hide under rocks or squeeze within bark for shelter, not only to survive hot and arid environments, but also to avoid crushing or pecking predation[11,14,20,21]. As such, they must resist external loading without damaging their internal organs (Fig. 2a). Analysis of the DIB by computed tomography (CT) reveals an air-filled region under the elytra known as the subelytral cavity, located above the abdomen (black space, Fig. 2a)[22]. Subsequent observations by CT and scanning electron microscope (SEM) of the ironclad's exoskeleton reveal three distinct lateral interfacial architectures that provide support between the elytra and ventral cuticle: interdigitated, latching and free-standing motifs (Fig. 2b). Additional CT scans show that these regions merge seamlessly into one another along the length of the body (Supplementary Video 2). In the other terrestrial beetles, a single large interdigitation remains persistent throughout their length (Extended Data Fig. 3j, o, t).

Simulations of the entire exoskeleton of the DIB under compression suggest that stress is concentrated at the perimeter of the cuticle, with load transferred to the ventral portion through the first and second types of lateral support described above (Extended Data Fig. 4e, f). Compression tests and finite element (FE) models of isolated sections demonstrate variations in stiffness and maximum displacement between supports (Fig. 2c, d). The first variant incorporates nearly complete sutural interdigitation, joining the elytra to the ventral cuticle and exhibiting the stiffest mechanical response. This highly integrated joint provides maximum protection to the thorax and vital organs by providing a fixed support at the base of the arched elytra to resist bending moments[23]. Mechanical testing and CT scans confirm that the maximum cross-sectional displacement before failure occurs is proportional to the height of the subelytral cavity. There is a 40.8% decrease in regional stiffness towards the posterior of the abdomen, concurrent with an average 165% increase in the vertical distance between the elytra and the organs.

The second and more posterior support incorporates a latching design that interlocks upon compression, allowing 40% greater displacement with minimal stress at the interface (Fig. 2c). In engineered structures, similar supports are incorporated in long bridges to allow for thermal expansion and contraction[23]. Closer inspection of the surfaces of the interfaces reveals an extensive array of 2 µm × 2 µm rod-like elements, known as microtrichia (Fig. 2b, Extended Data Fig. 5)[24]. Akin to the hair-like protuberances that flying beetles use to arrest their wings, the microtrichia from the DIB have a smaller aspect ratio (1:1 versus 1:5 in flying beetles) and probably provide a frictional grip to prevent slip during loading[25–27].

Supporting no load, the final interfacial variant (the posterior region of the elytra) lacks any true mechanical connection between the elytra and ventral cuticle. Two-dimensional (2D) FE models of the cuticle cross-section at different lateral support locations under compressive load indicate that the stress at any of the lateral interfaces is more than an order of magnitude lower than in the medial sutures (Fig. 2d). A 3D FE model of the cuticle under compressive load confirms that the stress substantially drops at the lateral supports for the free-standing variant versus those in the interdigitated case (Extended Data Fig. 4). We surmise that the free-standing and interlocking supports enable deflection of the elytra and therefore increase the energy absorption during crushing events by providing compliance, while the interdigitated supports increase stiffness.

Medial suture

Role of blade geometry and number

Repurposed for terrestrial living, the adapted ellipsoidal jigsaw blades in the elytron of *P. diabolicus* provide a mechanically interlocking joint between its two elytra (Fig. 3a). Similarly, other terrestrial beetles incorporate a single interlocking blade with a semicircular or triangular geometry to prevent separation of the elytra[28]. These interlocking sutures have been adopted as a strategy in many biological systems to regulate energy dissipation at interfaces and improve mechanical

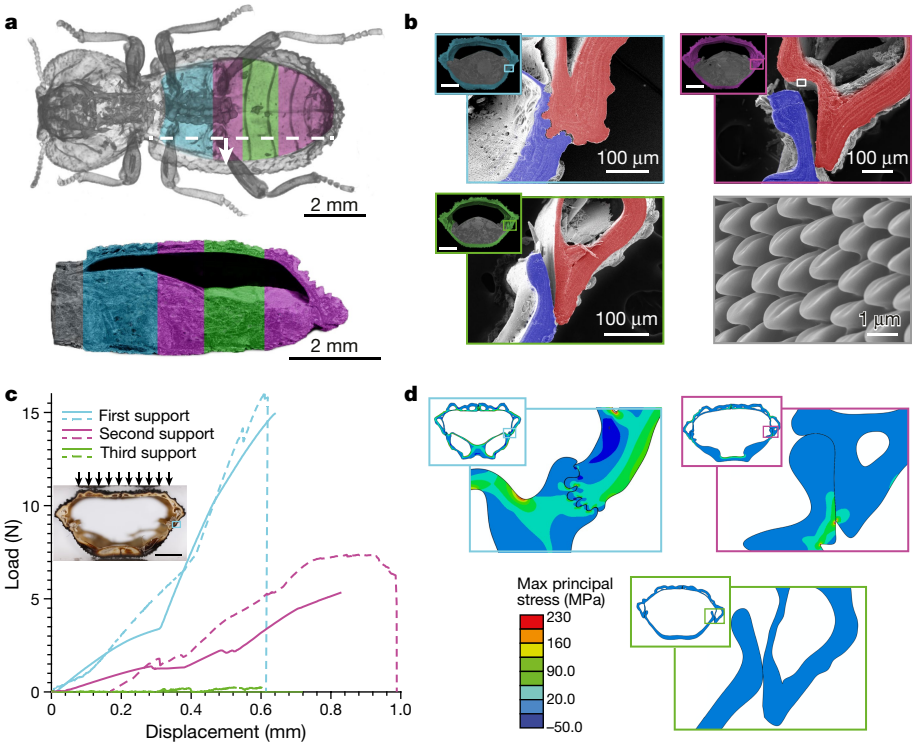

Fig. 2 | Role of regio-specific and graded lateral supports in the compression resistance of *P. diabolicus*. **a**, Plan view and longitudinal CT scans, highlighting three distinct internal regions with variable spacing between organs and elytra. **b**, False-coloured SEM images showing the distinct regional differences in interfaces between the elytra (red) and the ventral cuticle (blue). Bottom right, microtrichia providing frictional contact in contact region of the second support type (magenta shading in **a**). Insets, cross-sectional CT scans showing interface location. **c**, Compression load versus displacement curves of fully interdigitated (light blue), interlocking (magenta) and free-standing (green) lateral supports. Dashed lines represent experimental results; solid lines, simulation results. Inset, optical image of the fully interdigitated section used in the compression test. Scale bars, 2 mm. **d**, FE models of the stress distributions of the varied cross-sections and lateral supports during compression, highlighting the ability of the highly interlocked lateral supports to distribute load. Applied compressive displacement of 0.5 mm.

performance[29]. FE models incorporating the complex geometry of these interfacial structures in the DIB indicate a relatively uniform stress distribution across the suture due to their elliptical geometry and quantity (Fig. 3b). By contrast, beetles with one prime triangular or semicircular blade show larger principal stresses located in the necks and contact regions of these interdigitated structures. Geometric analysis of the *P. diabolicus* blades reveals a 1.8:1 ratio between the semi-major axis (b) and the focal point (a), with the primary geometry of each blade parametrically represented as three identical ellipses connected to each other at a specific angle θ, as defined in Fig. 3c. In the DIB, the contact angle is 25° between ellipses, yielding a mechanical interlock that prevents separation of elytra under tension (as is seen in circular elements)[30]. Furthermore, a uniform normal stress distribution at the blade interfaces enhances maximum tensile and shear stiffness, strength and fracture toughness[31]. Thus, we surmise that the elliptical geometry and the number of blades in the medial suture of *P. diabolicus* help to distribute stress uniformly and prevent rupture between mechanically interlocking elements.

Tensile tests of 3D-printed specimens and FE models reveal a linear trend between the number of blades and increased stiffness, toughness and normalized peak load of the medial suture (Extended Data Fig. 6). Evaluation of the role of the number of blades at a constant contact area provides further insight into the competing mechanisms between length scale and number of elements. Increasing the number of blades leads to a more uniform inelastic strain distribution, yielding properties reminiscent of a homogeneous material (higher stiffness at the cost of decreased extensibility; Fig. 3d). Tensile experiments and corresponding FE models indicate that the maximum toughness is found in sutures with two blades, whereas the maximum stiffness and peak load occur in samples with five and four blades, respectively (Fig. 3e and Extended Data Fig. 7). As fewer blade elements are used, there is a reduction in the inelastic strain concentration within the neck area of the blades. This inelastic strain distribution can explain the transition from ductile-like failure (pull-out with damage around the blades) to brittle-like failure (failure around the neck area) upon increasing the number of blades (or reducing their size; Extended Data Fig. 7). Additionally, a plot of maximum and minimum principal stress vectors (Extended Data Fig. 8) indicates that as the number of blades increases, there is an increase in compressive stress on the blades while a notably large tensile stress builds within the core of the neck. The compressive stress provides confinement as the number of the blades increases and, therefore, the highest stiffness can be expected for the sample with five blades. As the confinement increases, the tensile stress in the neck region increases. This leads to energy dissipation due to inelastic deformation to a point where brittle fracture at the neck becomes a competing mechanism. The sample with two blades does not display this behaviour and thus has the highest toughness.

Furthermore, as the volume of each element decreases, we see enhanced stiffness as the polymer chains are confined by localized contact loads at the bulbous regions[32]. This results in diminished strain and therefore reduced toughness as the polymer chains are confined to a small volume by the adjacent blades (Fig. 3e). Thus, as the quantity of elements over a constant contact area decreases, we see an increase in stiffness and uniform stress distribution.

Medial suture and microstructural effects

Closer examination of the cross-sections of the medial suture from the DIB (Fig. 4a) reveals a laminated architecture, which when placed

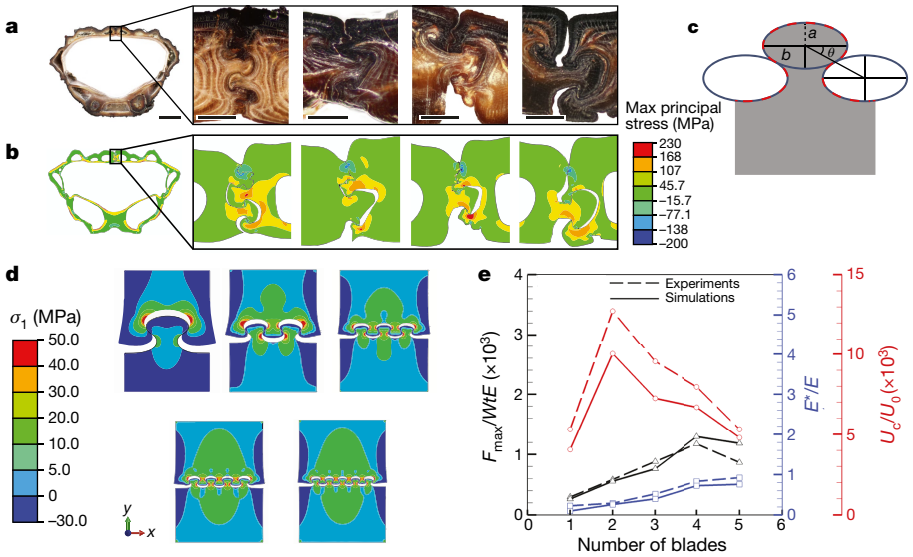

Fig. 3 | Role of suture blade geometry on mechanical performance. **a**, Optical micrographs of cross-sections of elytra from *P. diabolicus* (first and second from left). Comparing medial suture structures of *C. muricata*, *A. verrucosus* and *E. grandicollis*, respectively. **b**, FE models of the respective beetle sutures from **a**, showing stress distribution upon compression. Applied compression 0.5 mm. **c**, Blade geometry comprising three identical ellipses, inspired by the suture of *P. diabolicus*. **d**, FE models of samples tested in tension, showing stress distribution based on varying number of blade elements while keeping a constant contact area. **e**, Comparison between normalized peak load, stiffness and toughness for both 3D-printed tensile experiments and simulations. E, elastic modulus of the material; E^*, initial stiffness from load-displacement results; F, peak load; t, thickness of the sample; U_c, toughness (area under stress–strain curve); U_0, toughness of the base material; W, width of the sample.

under tensile loading shows failure in the matrix, highlighting local delamination (Fig. 4b). Charge contrast imaging shows the extent of delamination throughout the blades, suggesting an orchestrated stress release (Fig. 4c). With increased strain, CT scans demonstrate considerable delamination, with fibre bridging between layers (yellow arrows, Fig. 4d). Unlike homogeneous materials, which typically fail at their neck or thinnest feature[33], the microstructure within the blades enables considerable strain release and energy dissipation, circumventing catastrophic failure at the neck of the blades.

To understand the role of microstructural features and geometry of the blades, we developed three different 'jigsaw' geometries by varying the angle θ to 15°, 25° and 50° (Extended Data Fig. 9). In all three cases, the primary aspect ratios of the ellipses are constant and set equal to 1.8:1, and the 3D-printed jigsaw-shaped blades incorporate a layered architecture that mimics the DIB laminated microstructure (see Supplementary Methods). Tested in tension, the Lagrangian strains during loading are presented for all geometries (Extended Data Fig. 9). The 25° blades representing the DIB demonstrated higher normalized values of peak load and toughness (Fig. 4e). Digital image correlation (DIC) results confirm pull-out of the low-angle (15°) and nearly circular blade (Extended Data Fig. 9c), with no strain or delamination occurring. However, when θ is increased to 25° as in the DIB, a sizeable strain develops within the blade with subsequent delamination, followed by pull-out. Further tensile experiments and finite element modelling for the geometry specific to the DIB reveal the strain distribution and confirm the presence of delamination between layers before pull-out (Fig. 4f). Finally, in the highly curved blade ($\theta = 50°$), substantial strain is observed at the neck, followed by fracture (with no apparent delamination).

This analysis confirms the presence of competing mechanisms based on the jigsaw-like geometry and microstructure of the blades of the DIB. While the elliptical geometry provides maximum interlocking and strength at the suture, delamination within the microstructure of the blade prevents localized stresses that would cause failure at the neck, thus ensuring survival of this robust beetle.

Biomimetic sutures

As a type of mechanical fastener, the interfacial sutures of the DIB provide a robust joint and a more predictable failure than in other beetles. To test the potential advantages of this design as a mechanical fastener similar to those found in turbine engines or aerospace structures (for example dovetails in turbine blades or landing gear fittings)[2], we constructed a series of biomimetic composites with elliptical geometry and laminated microstructure. We tested these (under tensile loading) and compared them with chopped carbon strand and polymer-based blades along with a standard aerospace fastener (a Hi-Lok fastener that is used to join, for example, aluminium–carbon composite structures). Subsequent evaluation of strain distribution and strength, as well as energy dissipation (Fig. 4g and Extended Data Fig. 10), demonstrated that the composite blades mimicking the DIB suture are slightly stronger (about 19 ± 1.08 MPa) than current engineering fasteners (about 18 ± 0.73 MPa), yet demonstrate a substantial increase (more than 100%) in energy dissipation during displacement (158.0 ± 30.4 MPa mm versus 76.5 ± 1.4 MPa mm). DIC demonstrates a uniform distribution of stress within the blade (Fig. 4h), with localized delamination providing a means to avoid catastrophic failure at the neck, which occurs in both controls (that is, chopped carbon strand and polymer-based blades). The Hi-Lok fastener demonstrates a localized strain distribution around the pin connection and results in failure and separation of the plates. However, the laminated microstructure within the composite blade exhibits a more gradual failure, as delamination within the blade causes the neck of the structure to expand laterally, locking the structure instead of fracturing or narrowing and elongating before failure.

These designs could be useful in joining other dissimilar engineering materials such as plastics and metals. Such materials are currently joined by mechanical fastening, which adds weight and introduces stress concentrators that degrade the strength and can lead to fatigue issues, corrosion and early failure. There is considerable potential for further improvement of these interdigitated interfaces by tuning material parameters, which is being pursued.

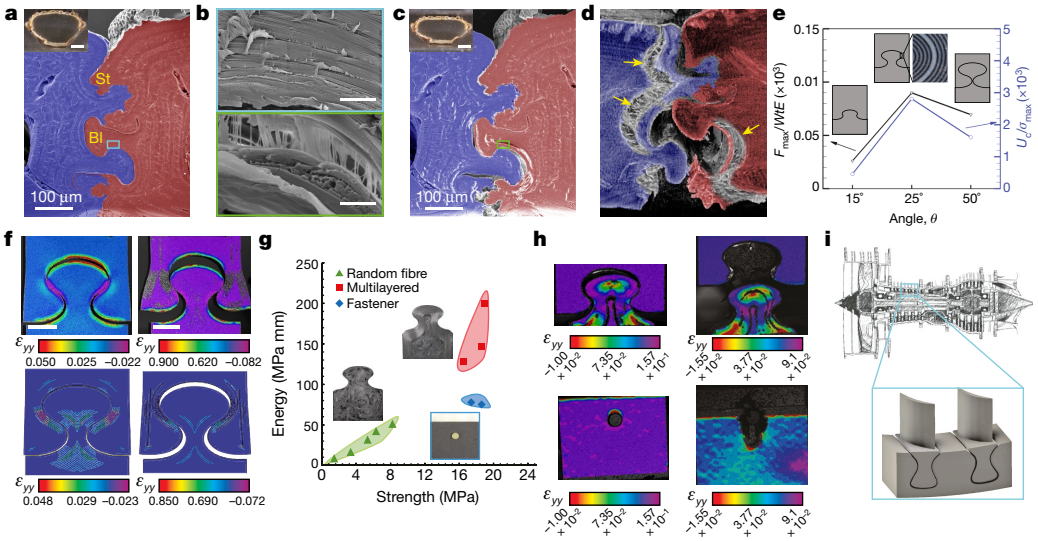

Fig. 4 | Role of microstructure in toughening of the medial suture. **a**, False-coloured SEM image of uncompressed transverse cross-section from the elytra of *P. diabolicus*. Bl, blades; St, stops. Inset, entire cross-section of uncompressed elytra. **b**, Laminated microstructure of blades before (top) and after (bottom) loading. **c**, Charge contrast and false-coloured SEM micrograph of compressed elytra, indicating crack initiation around blade regions depicted in **a**. Inset, entire cross-section of compressed elytra. **d**, CT reconstruction of fractured suture, revealing multiple failure points (yellow arrows), including fibre bridging and delamination in the structure. **e**, Comparison between normalized peak load and toughness of 3D-printed laminated blades with the angle θ set to 15°, 25° and 50°. **f**, Top, Lagrangian strain distribution using DIC, under tensile loading, of 3D-printed laminated blades with θ equal to 25°, showing strain developing within the blade and subsequent delamination. Bottom, FE simulations showing delamination and strain distribution. **g**, Ashby plot showing the strength and energy absorbance of composite-metal interfaces joined by laminated carbon fibre blades ('Multilayered'), randomly oriented chopped carbon fibre blades ('Random fibre') and titanium-based engineering fasteners. **h**, DIC showing variations in strain during tensile testing of composite-metal interfaces and revealing toughening mechanisms in laminated blades. **i**, Suture-like designs used in turbine blades.

Conclusions

Our studies reveal interfacial features in the elytra of *P. diabolicus* that assist the organism to withstand predation and other external loads. At the macroscale, the exoskeleton incorporates architecturally varied lateral supports, which yield stiffness gradients that protect vital organs and distribute load uniformly throughout the elytra. Further structural analysis and mechanical characterization of the elytra, coupled with FE simulations, highlight the benefits of geometry, number and microstructural features of an interdigitated suture. The ellipsoidal geometry and 25° contact angle between these sutural blades provide mechanical interlocking and diminish contact stress as compared with hemispherical and triangular analogues. Furthermore, a laminated microstructure provides toughening through delamination and fibre bridging at critical strains, avoiding catastrophic failure in the neck. A parametric study of blades, combining 3D printing and FE simulations, reveals that two blades provide the greatest toughness, whereas stress distribution, stiffness and peak load seem to be maximized with four blades. Biomimetic composites fabricated to mimic the DIB suture geometry and microstructure demonstrate an immediate benefit over aviation fasteners, providing enhanced strength and substantial increased toughness.

Online content

Any methods, additional references, Nature Research reporting summaries, source data, extended data, supplementary information, acknowledgements, peer review information; details of author contributions and competing interests; and statements of data and code availability are available at https://doi.org/10.1038/s41586-020-2813-8.

1. Martinsen, K., Hu, S. J. & Carlson, B. E. Joining of dissimilar materials. *CIRP Ann.* **64**, 679–699 (2015).
2. Jahn, J., Weber, M., Boehner, J. & Steinhilper, R. Assessment strategies for composite-metal joining technologies—a review. *Proc. CIRP* **50**, 689–694 (2016).
3. Wegst, U. G. K. & Ashby, M. F. The mechanical efficiency of natural materials. *Phil. Mag.* **84**, 2167–2186 (2004).
4. Hamilton, W. J. & Seely, M. K. Fog basking by the Namib Desert beetle, *Onymacris unguicularis*. *Nature* **262**, 284–285 (1976).
5. García-París, M., Coca-Abia, M. M. & Parra-Olea, G. Re-evaluation of the genera *Phloeodes*, *Noserus* and *Nosoderma* (Coleoptera: Zopheridae) with description of a new species of *Nosoderma* from northern México. *Ann. Soc. entomol. Fr.* **42**, 215–230 (2006).
6. Nickerl, J., Tsurkan, M., Hensel, R., Neinhuis, C. & Werner, C. The multi-layered protective cuticle of Collembola: a chemical analysis. *J. R. Soc. Interface* **11**, https://doi.org/10.1098/rsif.2014.0619 (2014).
7. Sun, J. & Bhushan, B. Structure and mechanical properties of beetle wings: a review. *RSC Adv.* **2**, 12606–12623 (2012).
8. Van De Kamp, T. & Greven, H. On the architecture of beetle elytra. *Entomol. heute* **22**, 191–204 (2010).
9. Foley, I. A. & Ivie, M. A phylogenetic analysis of the tribe Zopherini with a review of the species and generic classification (Coleoptera: Zopheridae). *Zootaxa* **1928**, 1–72 (2008).
10. Hunt, T. et al. A comprehensive phylogeny of beetles reveals the evolutionary origins of a superradiation. *Science* **318**, 1913–1916 (2007).
11. Baselga, A., Recuero, E., Parra-Olea, G. & García-París, M. Phylogenetic patterns in zopherine beetles are related to ecological niche width and dispersal limitation. *Mol. Ecol.* **20**, 5060–5073 (2011).
12. Frantsevich, L., Dai, Z., Wang, W. Y. & Zhang, Y. Geometry of elytra opening and closing in some beetles (Coleoptera, Polyphaga). *J. Exp. Biol.* **208**, 3145–3158 (2005).
13. Crowson, R. A. *The Biology of the Coleoptera* (Academic, 1981).
14. Polihronakis, M. & Caterino, M. S. Contrasting patterns of phylogeographic relationships in sympatric sister species of ironclad beetles (Zopheridae: *Phloeodes* spp.) in California's Transverse Ranges. *BMC Evol. Biol.* **10**, 195 (2010).
15. Miyatake, T., Katayama, K., Takeda, Y. & Nakashima, A. Is death-feigning adaptive? Heritable variation in fitness difference of death-feigning behaviour. *Proc. R. Soc. B* **271**, 2293–2296 (2004).
16. Rider, S. D. Jr. The complete mitochondrial genome of the desert darkling beetle *Asbolus verrucosus* (Coleoptera, Tenebrionidae). *Mitochondrial DNA A* **27**, 2447–2449 (2016).
17. Triplehorn, C. A. A synopsis of the genus Cryptoglossa Solier (Coleoptera: Tenebrionidae). *Coleopt. Bull.* **18**, 43–52 (1964).
18. Astin, A. D. *Finger Force Capability: Measurement and Prediction Using Anthropometric and Myoelectric Measures*. PhD thesis, Virginia Polytechnic Institute and State Univ. (1999).
19. Dai, Z., Zhang, Y., Liang, X. & Sun, J. Coupling between elytra of some beetles: mechanism, forces and effect of surface texture. *Sci. China C* **51**, 894–901 (2008).
20. Schilman, P. E., Kaiser, A. & Lighton, J. R. B. Breathe softly, beetle: continuous gas exchange, water loss and the role of the subelytral space in the tenebrionid beetle, *Eleodes obscura*. *J. Insect Physiol.* **54**, 192–203 (2008).

21. Doyen, J. T. Description of the larva of *Phloeodes diabolicus* LeConte (Coleoptera: Zopheridae). *Coleopt. Bull.* **30**, 267–272 (1976).
22. Draney, M. L. The subelytral cavity of desert tenebrinoids. *Fla Entomol.* **76**, 539–549 (1993).
23. Connor, J. J. & Faraji, S. *Fundamentals of Structural Engineering* 2nd edn (Springer, 2016).
24. Guo, C., Song, W. W. & Dai, Z. D. Structural design inspired by beetle elytra and its mechanical properties. *Chin. Sci. Bull.* **57**, 941–947 (2012).
25. Enders, S., Barbakadse, N., Gorb, S. N. & Arzt, E. Exploring biological surfaces by nanoindentation. *J. Mater. Res.* **19**, 880–887 (2004).
26. Gorb, S. N. et al. Structural design and biomechanics of friction-based releasable attachment devices in insects. *Integr. Comp. Biol.* **42**, 1127–1139 (2002).
27. Gorb, S. N. Frictional surfaces of the elytra-to-body arresting mechanism in tenebrinoid beetles (Colioptera: Tenebrionidae): design of co-opted fields of microtrichia and cuticle ultrastructure. *Int. J. Insect Morphol. Embryol.* **27**, 205–225 (1998).
28. Lin, E., Li, Y., Ortiz, C. & Boyce, M. C. 3D printed, bio-inspired prototypes and analytical models for structured suture interfaces with geometrically-tuned deformation and failure behavior. *J. Mech. Phys. Solids* **73**, 166–182 (2014).
29. Hosseini, M. S., Cordisco, F. A. & Zavattieri, P. D. Analysis of bioinspired non-interlocking geometrically patterned interfaces under predominant mode I loading. *J. Mech. Behav. Biomed. Mater.* **96**, 244–260 (2019).
30. Mirkhalaf, M. & Barthelat, F. Design, 3D printing and testing of architectured materials with bistable interlocks. *Extreme Mech. Lett.* **11**, 1–7 (2017).
31. Malik, I. A. & Barthelat, F. Bioinspired sutured materials for strength and toughness: pullout mechanisms and geometric enrichments. *Int. J. Solids Struct.* **138**, 118–133 (2018).
32. Tweedie, C. A. et al. Enhanced stiffness of amorphous polymer surfaces under confinement of localized contact loads. *Adv. Mater.* **19**, 2540–2546 (2007).
33. Malik, I. A., Mirkhalaf, M. & Barthelat, F. Bio-inspired 'jigsaw'-like interlocking sutures: modeling, optimization, 3D printing and testing. *J. Mech. Phys. Solids* **102**, 224–238 (2017).

Methods

Specimen handling and sample preparation

Research specimens: live specimens of *P. diabolicus* (0.43 ± 0.13 g; 21.3 ± 3.7 mm length; 5.3 ± 1.1 mm height), *A. verrucosus*, *E. grandicollis* and *C. muricata* were acquired from the University of California Riverside campus and a series of local collectors. Before experimentation, beetles were housed in a terrarium at room temperature (25 °C). Elytra were obtained from recently killed specimens. For optical characterization, samples were embedded in epoxy resin (System 1618, Polymer Composites), sectioned using a Techcut 4 low speed saw with a diamond blade (Allied), and polished progressively down to a 0.05 µm roughness with diamond abrasive (Allied). Cross-sections were obtained in transverse and longitudinal directions. Fractured samples of the elytra were prepared by breaking with forceps.

Mechanical testing

Exoskeletal compression tests were conducted on euthanized and dehydrated samples using a Bose ElectroForce 3200 Series III Test Instrument at a rate of 0.01 mm s^{-1} between two steel plates. Samples were tested until failure of the exoskeleton (fracture of the suture) and the peak load was measured. Five samples of each species of beetle were tested. Compression tests were conducted on selected 2 mm cross-sections obtained from recently deceased specimens by using a Techcut 4 low-speed saw with a diamond blade (Allied). The sections were distinguished by the varying lateral supports of *P. diabolicus*. Samples from each section were compressed with a Bose ElectroForce 3200 Series III Test Instrument at a rate of 0.01 mm s^{-1}.

Micro computed tomography

Micro-CT scans were conducted at the Advanced Light Source at Lawrence Berkeley National Laboratory (BL 8.3.2). Samples were imaged (continuous mode, 1,025 projections, 180° rotation) with a monochromatic X-ray energy of 17 keV with a 10 mm distance from sample to scintillator and a 700 ms exposure. The 1× and 10× objectives were used, resulting in a pixel size of 6.5 µm and 0.65 µm, respectively. Volumes were reconstructed using the Xi cam software developed at the Advanced Light Source facility.

Full specimens were studied using X-ray micro-tomography in a SkyScan 1076 at 250 µA and 40 kV with no filter. N-Recon Software (Bruker) was used for reconstruction. Scans were visualized using CT Vox (Bruker) and Amira (Thermo Fisher Scientific).

Organic component analyses

Elytra obtained from *P. diabolicus* and *T. dichotomus* were dried at 60 °C for 24 h and were weighed. Lipids were extracted from dried elytra with 1 ml of ethyl ether for 24 h at room temperature. This treatment was repeated three times. After removal of solvent, elytra were dried for 3 h and were then weighed. The elytra were deproteinized in a 1 M sodium hydroxide solution for 1 h at 85 °C. This was repeated several times until the protein concentration in the extracted solution was below the detectable limits of a BCA assay. The resulting elytra, which had a white colour, were dried for 24 h at 60 °C. The weight was determined as the chitin content in the elytra. Lipid content was calculated from the difference of weights between untreated dried elytra and dried elytra after lipid extraction. Protein content was determined from the difference in weight between dried elytra after lipid extraction and dried deproteinized elytra. Differences in protein profiles between *P. diabolicus* and *T. dichotomus* elytra can be seen in Supplementary Fig. 1.

Scanning electron microscopy

Fractured and polished samples were sputter-coated with platinum/palladium (Cressington 108 Auto, CFAMM UCR) and examined in the SEM (Philips XL 30, CFAMM UCR).

Nanoindentation

Mechanical properties used in FE modelling were obtained from nanoindentation of the beetle cuticle. Recently deceased samples were embedded in epoxy (System 1618, Polymer Composites) cut to a 5 mm thickness, adhered to a steel AFM puck and polished to 0.05 µm roughness. Indentation was performed on polished flat cross-sections of the exoskeleton at room temperature with a TI 950 Triboindenter (Hysitron). Detailed indentation maps were performed using a low load transducer with a Berkovich tip. Indentation maps were performed in the regions of interest. Displacement controlled tests were performed to a 300 nm depth of nanoindenter tip and a load function consisting of a 5 s load, followed by a 2 s hold and a 5 s unload. Values for reduced elastic modulus and hardness were calculated by the Oliver and Pharr method. Spatial maps of reduced modulus and hardness were subsequently plotted with the scatter function in MATLAB (MathWorks).

Topography and roughness

Surface roughness and topography maps of the elytra were obtained for *P. diabolicus* and *T. dichotomus* by using the scan mode in the VK-X150 (Keyence) 3D laser scanning microscope with an objective lens (10×). Results from the scans can be seen in Supplementary Fig. 2.

FE modelling of elytra and 3D laminated samples

2D sections. 2D optical images of a transverse cross-section of the DIB showing the medial sutures and the lateral supports were digitized in the FE software Abaqus for its analysis. The models were meshed using 65,217 four-node plane strain elements (CPE4 in Abaqus). An elastic–plastic model was assumed for the simulations with a Young's modulus $E = 9.45 \pm 3.16$ GPa, obtained from nanoindentation (Extended Data Fig. 2); Poisson's ratio $\nu = 0.3$; and a plasticity power law following $\sigma = \sigma_y(E/\sigma_y)^{\mu}\varepsilon^{\mu}$, where σ_y and μ were inversely calculated from the experimental data corresponding to 100 and 0.1, respectively. The models were compressed between two rigid analytical surfaces. The contact between the plates and the sections of the elytra was assumed frictionless and rigid (that is, no penetration is allowed). The bottom surface was assumed fixed, while displacement control was applied to the top surface. Force–displacement curves were obtained by by measuring from a reference point located in the top surface. The same model was using for comparing the medial sutures of different beetles. In this case, the medial sutures of *C. muricata*, *A. verrucosus* and *E. grandicollis* were digitized with Abaqus and scaled to fit in the cross-section of the DIB; the other simulation parameters were kept constant.

Abdomen 3D model. 3D micro-CT scans of the entire abdomen of the DIB were used to create the 3D CAD geometries and meshed using Amira. Both geometry and meshes were transferred to Abaqus for further analysis. The entire abdomen consists of 1,458,337 linear tetrahedral elements (C3D4 in Abaqus). Material is assumed to be elastic with Young's modulus $E = 9.45 \pm 3.16$ GPa and Poisson's ratio $\nu = 0.3$ (Extended Data Fig. 2). The abdomen model is then compressed between two rigid analytical surfaces. The bottom surface is fixed, and displacement control is applied to the top surface. The contact between the rigid plates and the abdominal parts was assumed to be frictionless and rigid.

3D printing and mechanical testing of blades. 3D-printed samples were fabricated by a Formlabs Form 2 stereolithography printer and their proprietary tough resin (TOTL04) at a layer thickness of 0.05 mm with a final part geometry of 40 × 55 × 5 mm. The samples were post-cured under a 405 nm light at 60 °C for 120 min, according to manufacturer specifications. Tensile tests were conducted on an Instron 5969 Dual Column Testing System in accordance with adapted ASTM D638 standards and at a rate of 0.05 mm s^{-1}. Mechanical properties for the resin samples were obtained by tensile tests conforming to ASTM D638 standards; ($N = 5$), $E = 1.7 \pm 0.1$ GPa, $\sigma = 34 \pm 1.9$ MPa (mean ± s.d.).

Parametric blade modelling. 2D FE models of the 3D-printed blade specimens were developed by using Abaqus. The material is assumed to be elastic–perfectly plastic with $E = 1{,}700$ MPa, $\nu = 0.22$, $\sigma_y = 34$ MPa and the fracture strain $\varepsilon_f = 0.35$. The material properties for resin were adopted from the previous section. For all jigsaw blades, displacement load-control is applied on the top surface of the female part, and the bottom surface in the male part is fixed against displacements and rotations.

3D printing and mechanical testing of laminated blades. Tensile tests were conducted on the 3D-printed samples of blades inspired by the ironclad beetle macro- and microstructures. 3D-printed samples were fabricated by a Connex 350 3D printer with two base materials. The 3D-printed samples contain layers of VeroWhite (thickness of 1.2 mm) connected by TangoBlack interfaces (thickness of 0.6 mm). Three different models were developed and tested by varying the angle θ to 15°, 25° and 50° (Extended Data Fig. 9). The out-of-plane thickness of all samples was equal to 12 mm. The tensile tests were conducted on the MTS Testing System along with DIC in accordance with ASTM D638 standards. Test were conducted at a rate of 0.05 mm s^{-1} for all samples.

Modelling laminated blades

A 3D FE model of jigsaw-puzzle-like blade, similar to the 3D-printed laminated samples in previous section, was developed for $\theta = 25°$ in Abaqus (Extended Data Fig. 8a, and Fig. 4f. The model consists of alternating layers of VeroWhite and TangoBlack polymer. The VeroWhite characteristics are taken from the ASTM D638 standards. The TangoBlack polymer is characterized by performing three tests: (i) tensile tests; (ii) double cantilever beam (DCB) tests using ASTM D5528 to obtain the mode-I properties; and (iii) end notch flexure tests (ENF) using ASTM D7905 to characterize the mode-II behaviour. By using the force–displacement curves from these experiments and reverse engineering from FE simulations, we were able to obtain the material properties of both polymers. In our simulations, the VeroWhite polymer is assumed to be elastic–perfectly plastic with Young's modulus $E = 950$ MPa, $\nu = 0.22$, $\sigma_y = 60$ MPa and $\varepsilon_f = 0.35$. The TangoBlack polymer is modelled using the traction-separation law model and the normal stress $\sigma_{max} = 2.0$ MPa with mode-I energy, $G_I = 2$ MPa m, and the shear stress $\tau_{max} = 0.65$ MPa, with mode-II energy equal to $G_{II} = 0.6$ MPa m. The boundary and loading conditions are similar to those described in the previous section. The material properties obtained for TangoBlack and VeroWhite were used in the FE simulations (Extended Data Fig. 9).

The 3D-printed samples were fabricated with Connex 350 and cured for a week after the print in accordance with the manufacturer's specifications. We carried out tensile tests on dogbone coupon samples made of VeroWhite and TangoBlack in accordance with ASTM D638 and at a rate of 0.05 mm s^{-1}, which was deemed to be slow enough to avoid strain-rate dependence of the polymers. Since the TangoBlack is used as an adhesive to connect VeroWhite layers in the puzzle-like blades (Extended Data Fig. 9b), we conducted two types of experiment (DCB and ENF tests) to characterize the fracture properties. The DCB sample consists of two VeroWhite rectangular plates with a TangoBlack midplane acting as the adhesive. The geometry and test set-up followed ASTM D5528. Opening forces are applied to the end of the DCB specimen through a special tab that was bonded near the ends of the specimen. The load is applied by controlling the crosshead movement of the MTS tensile testing machine, while the load and delamination length are recorded.

While the DCB samples were used to characterize the mode-I energy release rate, ENF provides the mode-II energy release rate. The ENF samples were 3D-printed based on ASTM D7905, and consists of two rectangular, uniform thickness VeroWhite plates with the TangoBlack adhesive as the midplane. The specimen is then subjected to three-point bending using displacement control. The results from the load–displacement curves enabled calculation of mode-II energy-release rates through an iterative process using FE analysis to determine the main cohesive properties.

Biomimetic composite blade fabrication and testing

Composite blade samples used a 25° contact angle between segments and were manufactured using 85 g per square metre unidirectional carbon fibre pre-impregnated with toughened epoxy (AX-6201XL-C-85GT700-24″ RC34, Axiom). The lay-up architecture consisted of 30 layers of unidirectional fibre, circumferentially wrapped around a core of chopped graphite fibre (571-A, Fibreglast). The final dimensions were $8 \times 45 \times 49$ mm^3.

Two additional sets of biomimetic blades were fabricated: (i) randomly oriented composite blades were fabricated from 1/4″ chopped graphite fibre (50 vol%, 571-A, Fibreglast) and epoxy (System 1618, Polymer Composites) and (ii) epoxy blades (no fibre reinforcement) were fabricated using epoxy resin (System 1618, Polymer Composites). Both sets were cured in a custom mould for consistent dimensions. Finally, a female fixture was machined out of aluminium 6061-T6.

Mechanically fastened samples used titanium Hi-Lok Pins (HL10VAZ6-3) fastened by aluminium Hi-Lok Collar (HL79-62024) to secure a quasi-isotropic 3k (that is, 3,000 filament) 13-ply plain weave panel to an aluminium 6061-T6 plate. All samples were sectioned to meet the dimensional standards with four duplicates of each produced for statistics of mechanical testing and structural characterization.

Tensile tests were conducted with the MTS tensile testing machine on blade samples composed of epoxy, randomly orientated chopped-strand graphite fibre, laminated carbon fibre as well as Hi-Lok fastened samples. All the tests were conducted at a rate of 0.01 mm s^{-1} to satisfy the quasi-static loading condition. The DIC method is also used during the experiments for better insight into the failure mechanism of each system. Tests were continued until full separation occurred.

Data availability

The data that support the findings of this study are available from the corresponding author on reasonable request. Source data are provided with this paper.

Acknowledgements This research was supported by grants from AFOSR, Multi-University Research Initiative, award FA9550-15-1-0009 (D.K.) Electron microscopy was conducted at the Central Facility for Advanced Microscopy and Microanalysis (CFAMM). D.K. thanks the Army Research Office DURIP grant (W911NF-16-1-0208) for the MIRA SEM. P.Z. thanks the AFOSR DURIP grant (FA2386-12-1-3020) for the 3D printer. A.A. and D.K. thank the Institute of Global Innovation Research (GIR) at TUAT for their support. This research used resources of the Advanced Light Source, which is a DOE Office of Science User Facility under contract no. DE-AC02-05CH11231. We also acknowledge M. Cooper for helping with CAD drawings of laminated blades.

Author contributions J.R. conducted mechanical and ultrastructural characterization of the beetle cuticles. J.R. and D.K. analysed ultrastructural and mechanical characterization results. J.R. and M.S.H. prepared 3D-printed samples. M.S.H., D.R. and P.Z. carried out the FE simulations and assisted with data analysis. J.R., S.M. and A.A. performed chemical analysis of the beetle cuticles. D.Y.P. and H.S.B. provided assistance in acquiring CT scans. D.V. assisted in the fabrication of the laminated composite blades. D.K. planned and coordinated project and experimental tasks. All authors contributed to the writing of the manuscript.

Competing interests The authors declare no competing interests.

Additional information
Supplementary information is available for this paper at https://doi.org/10.1038/s41586-020-2813-8.
Correspondence and requests for materials should be addressed to D.K.
Peer review information *Nature* thanks Po-Yu Chen, Patrick Fairclough and Richard Johnston for their contribution to the peer review of this work.
Reprints and permissions information is available at http://www.nature.com/reprints.

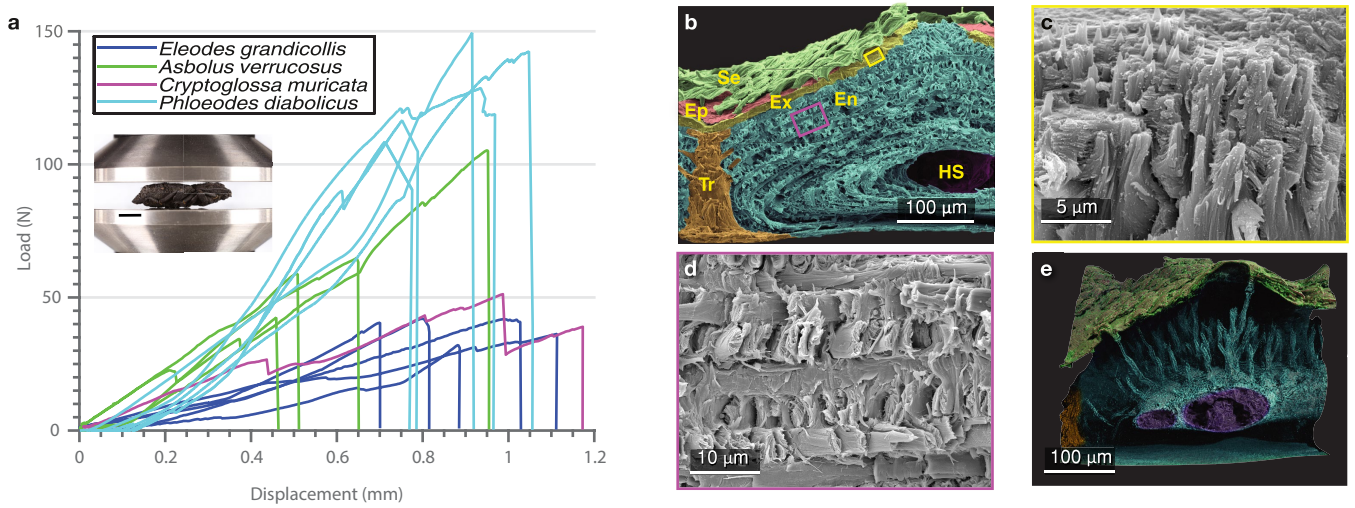

Extended Data Fig. 1 | Compression results for beetles tested. a, Force versus displacement curves for all samples tested in compression, $N = 5$. Inset, image of compression test apparatus, with recently deceased sample mounted between two parallel steel plates. Scale bar, 5 mm. **b**, False-coloured SEM micrograph of fractured cross-section of the elytra, highlighting leaf-like setae (Se, green), epicuticle (red), exocuticle (Ex, yellow), endocuticle (En, blue), trabecula (Tr, orange) and haemolymph space (HS, violet). **c**, SEM micrograph of fractured exocuticle (yellow box in **a**), showing through-ply thickness fibres. **d**, SEM micrograph of endocuticle (purple box in **a**), revealing pseudo-helicoidal fibre orientation. **e**, Micro-CT reconstruction of elytra revealing internal pore canal network that leads to internal network of haemolymph space (highlighted in purple).

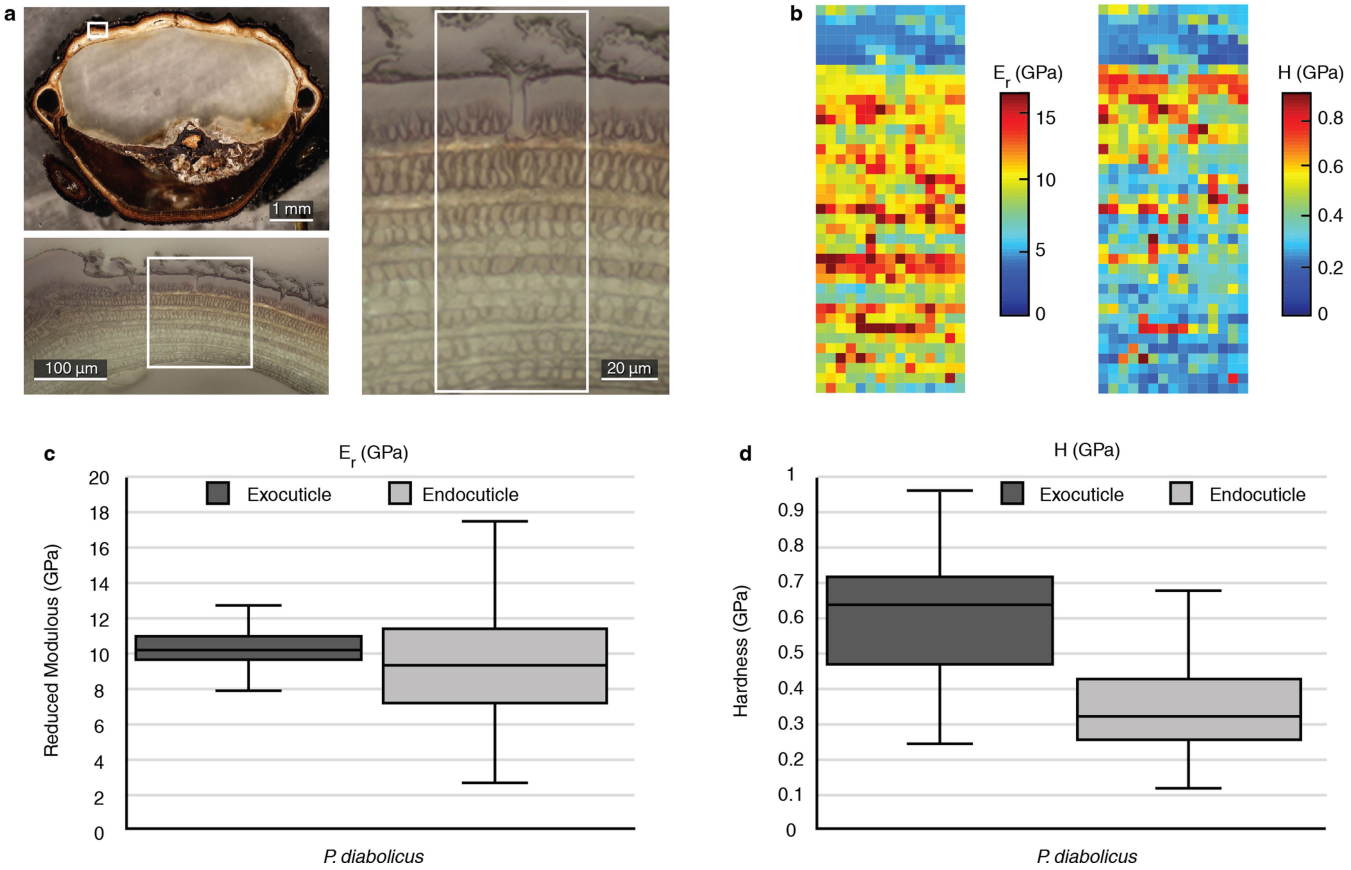

Extended Data Fig. 2 | Indentation analysis of the endocuticle of *P. diabolicus*. **a**, Cross-section of *P. diabolicus* highlighting the exo- and endocuticle of the elytra. **b**, High-resolution surface map of exo- and endocuticle obtained with a Berkovich tip, indicating the reduced elastic modulus and hardness results from the elytra. **c**, **d**, Plots showing the variation between the reduced elastic modulus (**c**) and hardness (**d**) of the exo- and endocuticle.

Extended Data Fig. 3 | Variations in macro- and microstructures in desert beetles and a flying beetle. a–**u**, Column 1: overview of insect; column 2: elytra of organism; column 3: cross-sections (scale bars, 1 mm); column 4: suture that binds the two elytra (scale bars, 100 µm); column 5: lateral support interfacing elytra to the ventral cuticle (scale bars, 100 µm). Rows (top to bottom): **a**–**e**, *P. diabolicus*, **f**–**j**, *A. verrucosus*, **k**–**o**, *C. muricata*, **p**–**t**, *E. grandicollis*, **u**–**x**, *T. dichotomus* (scale bars in columns 1 and 2, 5 mm).

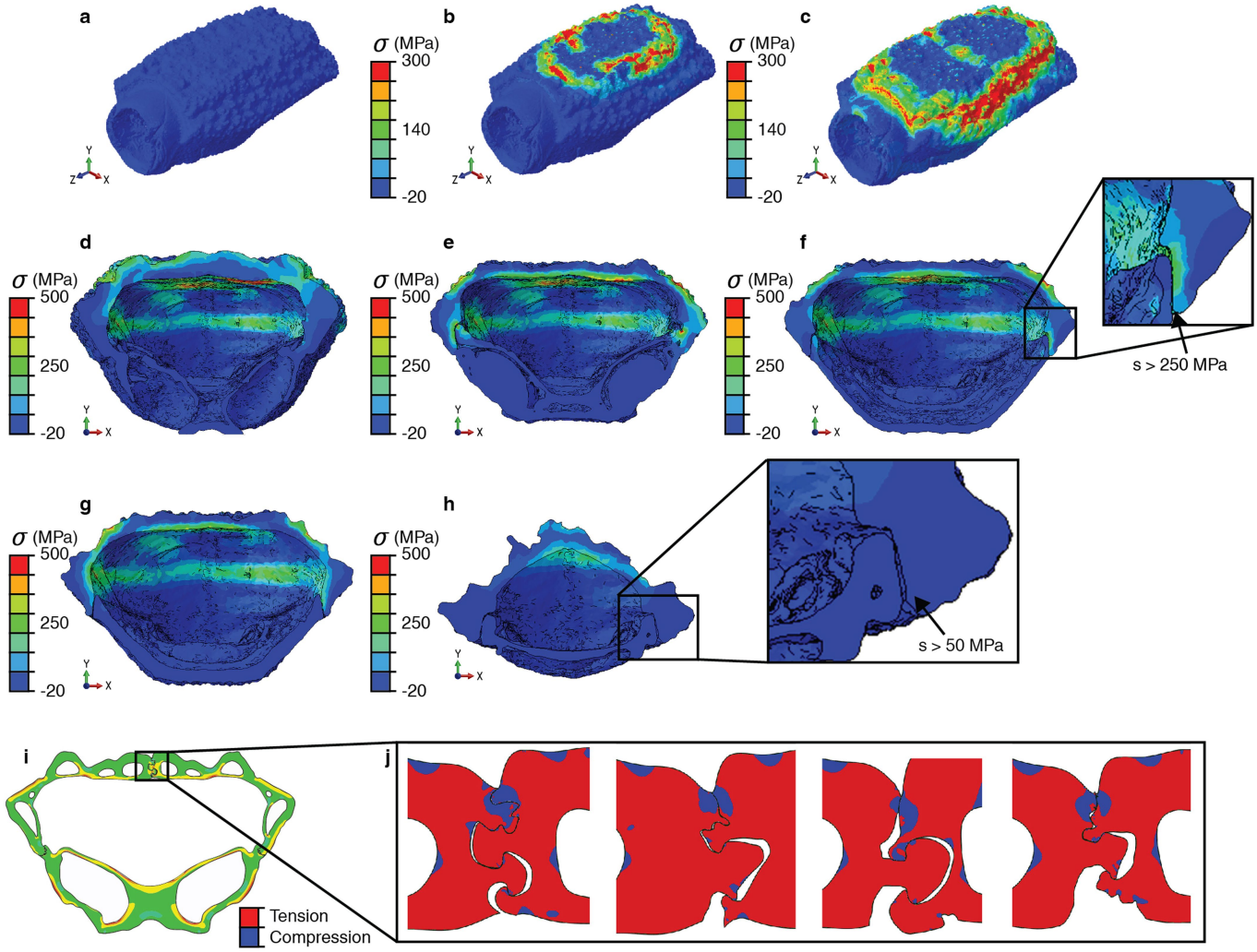

Extended Data Fig. 4 | FE models of elytra under compression. a, Model of the elytra and abdomen. **b**, Initial displacement of the elytra showing principal stresses at contact location. **c**, Increased displacement of elytra showing the distribution of principal stresses. **d**–**h**, Cross sections of **c** highlight principal stresses at first lateral support (**d**), second lateral support (**e**, **f**), third lateral support (**g**) and repetition of second support at the posterior of the abdomen to prevent collapse of the elytra (**h**). **i**, FE model of cross-section under compression. **j**, FE model of suture region, indicating the dominance of tensile forces while under load. Applied compressive displacement of 0.5 mm.

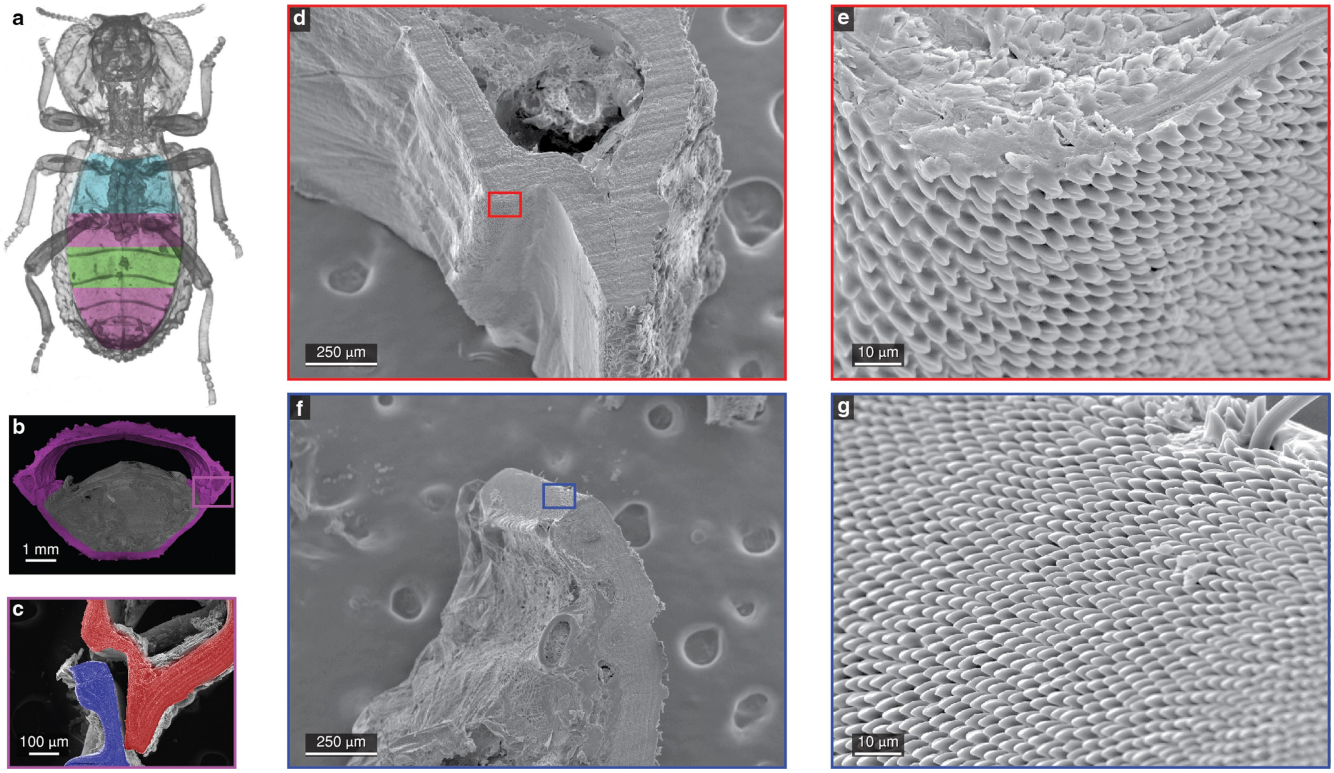

Extended Data Fig. 5 | Frictional microtrichia located at the interfaces between the elytra and ventral cuticle. a, CT scans, highlighting three distinct internal regions. **b**, **c**, CT scan cross-section of the second support (**b**), with magnification (**c**) indicating the interface between the elytra and ventral cuticle. **d**–**g**, SEM micrograph (**d**) of the elytra interface, indicating microtrichia (**e**) that provide frictional contact between **d** and **f**, the ventral cuticle with its surface (**g**) also coated with microtrichia.

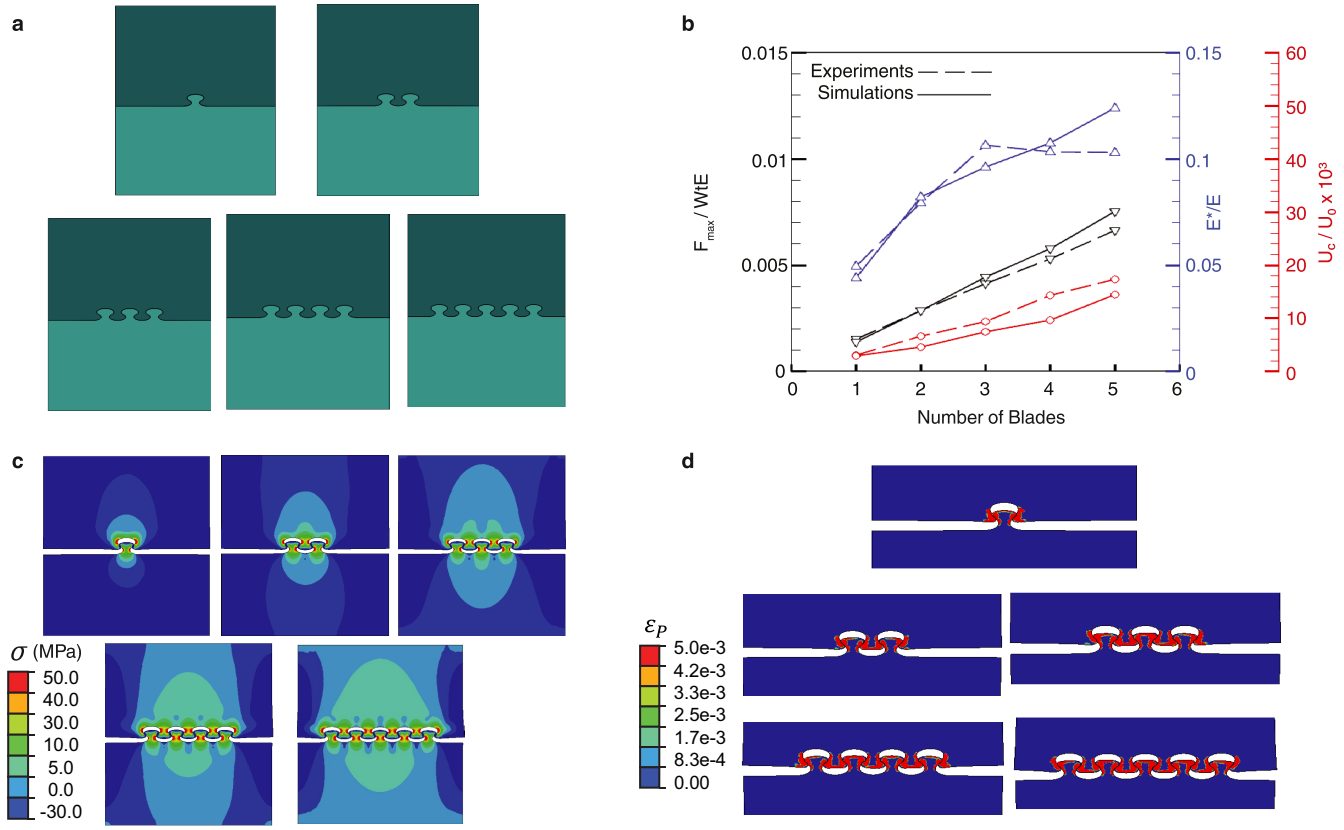

Extended Data Fig. 6 | Mechanical response on increasing the number of blades. a, Parametric tensile samples, inspired by the natural system, with one to five blades. **b**, Comparison between normalized peak load, stiffness and toughness from 3D-printed tensile experiments and simulations. **c**, FE tensile simulations of sutural quantity variation, showing stress distribution based on number of elements. **d**, FE models showing maximum strain in blades subjected to tensile loads.

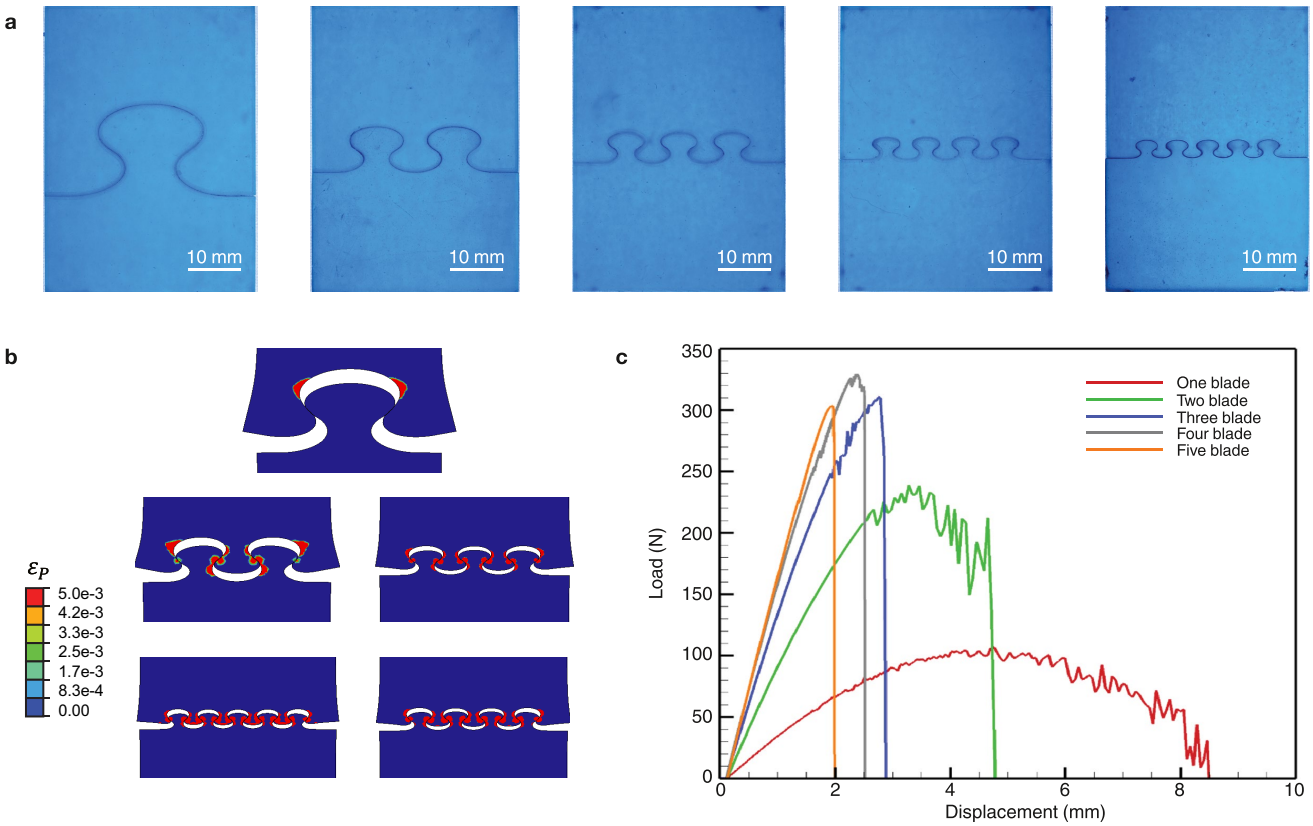

Extended Data Fig. 7 | Mechanical response of suture with increasing number of blades but constant contact area between elements. a, Printed samples produced for mechanical testing. **b**, FE models showing maximum strain in blades subjected to tensile loads. **c**, Representative load versus displacement curves for tested samples.

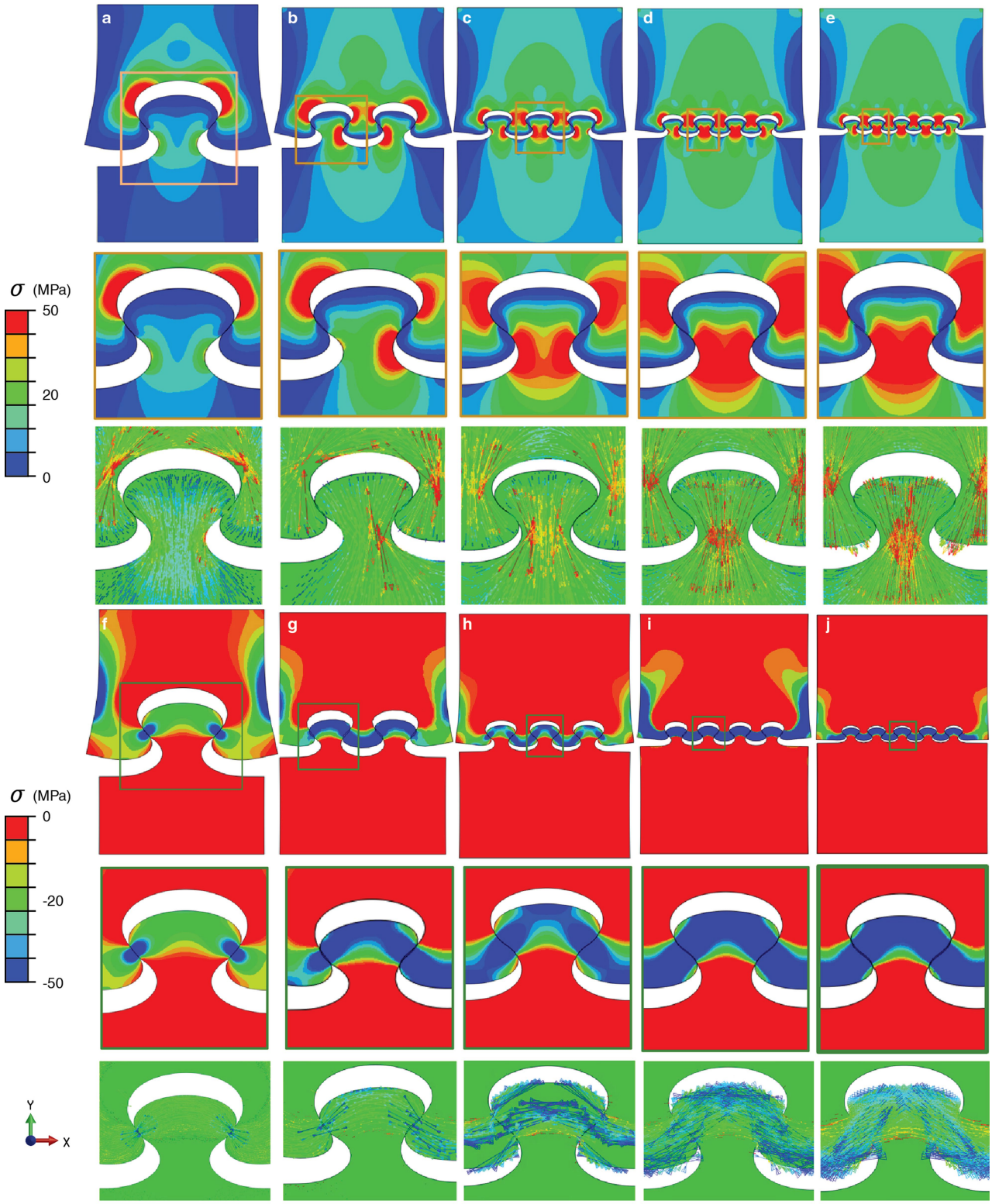

Extended Data Fig. 8 | Tensile and compressive stresses as a function of number of blades. a–**e**, First row: maximum principal stress contours for one (**a**), two (**b**), three (**c**), four (**d**) and five (**e**) blades at the point of maximum load. Second row: highlighted stress within the central blade for each set of experiments in the top row. Third row: distribution of the principal directions associated with the maximum principal stress. **f**–**j**, First row: minimum principal stress contours for one (**f**), two (**g**), three (**h**), four (**i**) and five (**j**) blades at the point of maximum load. Second row: highlighted stress within the central blade for each set of experiments in the row above. Third row: distribution of the principal directions associated with the minimum principal stress.

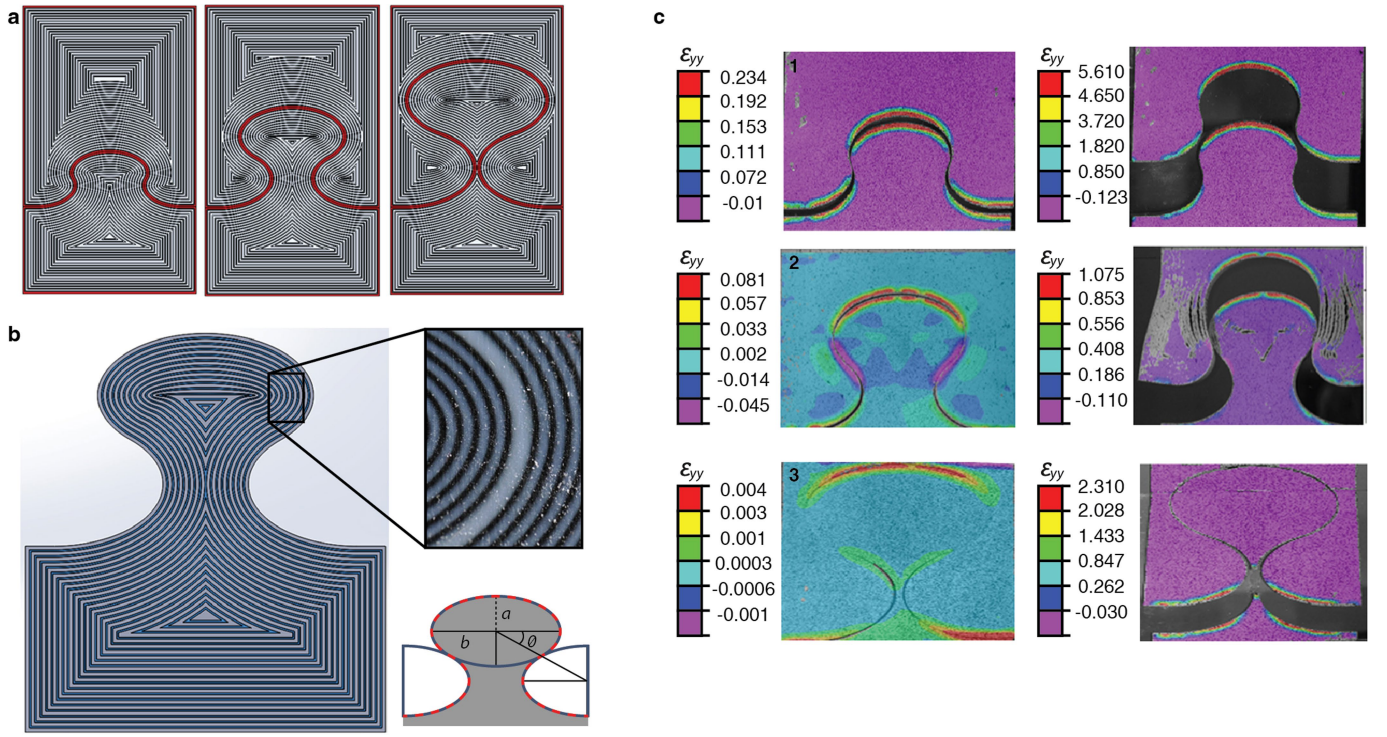

Extended Data Fig. 9 | Additive manufactured laminated blades. a, Three different jigsaw geometries developed by varying θ to 15°, 25° and 50°. **b**, Multi-material additively manufactured jigsaw blades containing 1.2-mm-thick VeroWhite layers bonded together with 0.6-mm-thick TangoBlack Plus. Inset shows the architecture inside each blade. **c**, Tensile tests of 3D-printed specimens with DIC, indicating localized strain that leads to failure mechanisms including pull-out, delamination and fracture.

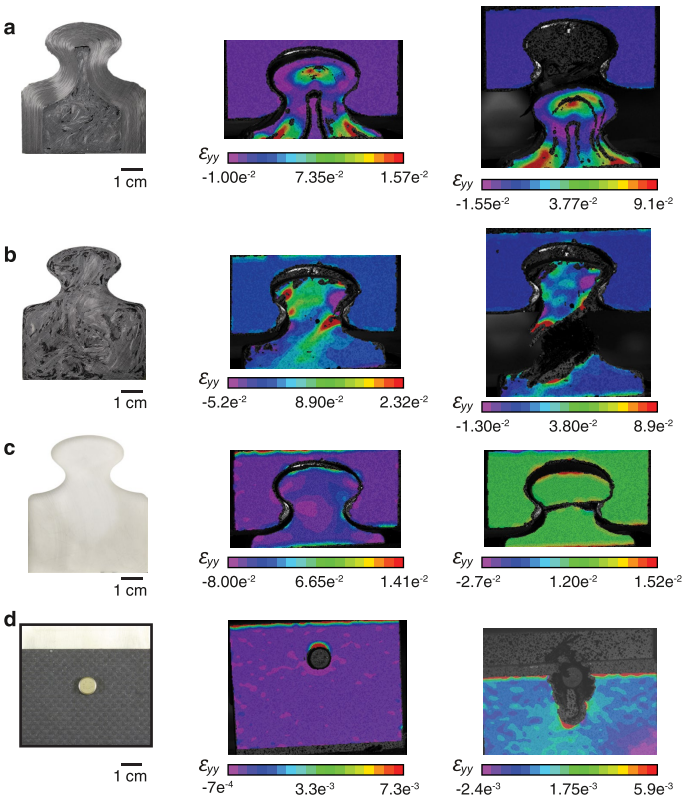

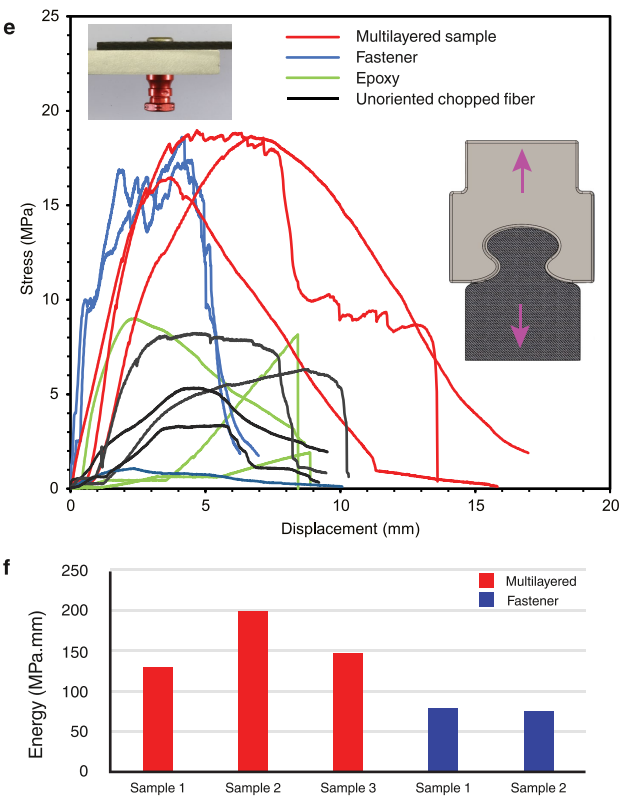

Extended Data Fig. 10 | Tensile test of composite blades and engineering fasteners. a–**d**, Images of sample (left); DIC of strained sample (centre); and DIC of fractured sample (right). **a**, Composite blade composed of circumferentially laminated pre-impregnated carbon fibre with a core made of chopped graphite fibre plus epoxy. **b**, Composite blade composed of unoriented chopped-strand graphite fibres in an epoxy matrix. **c**, Epoxy blade. **d**, Titanium Hi-Lok fastener binding a plane-weave carbon fibre epoxy panel to a 6061-aluminium plate. **e**, Stress versus displacement curves indicating the tensile response of the laminated blades (from **a**) and engineering fastener (from **d**). **f**, Energy absorbed by each composite before failure.